A 3-DoF Experimental Test-Bed for Integrated Attitude Dynamics and Control Research

Dongwon Jung* and Panagiotis Tsiotras†
School of Aerospace Engineering
Georgia Institute of Technology, Atlanta, GA 30332-0150

This article presents the details of a newly constructed 3-dof experimental spacecraft simulator facility at the School of Aerospace Engineering at the Georgia Institute of Technology. The main component of the facility is a cylindrical platform located on a hemi-spherical air bearing that allows friction-free rotation about three axes. The facility includes a variety of actuators and sensors: gas thrusters, variable-speed controlled momentum gyros (which can operate solely in a reaction wheel (RW) or in a control momentum gyro (CMG) mode), a two-axial sun sensor, a high-precision three-axial rate gyro, a three-axial magnetometer, and a complementary inertial measurement unit. The facility offers a truly integrated attitude control system (IACS) for experimental testing of advanced attitude determination and control algorithms.

Introduction

This article presents the details of a newly designed spacecraft simulator facility at the School of Aerospace Engineering at the Georgia Institute of Technology. The simulator is a second-generation facility evolved from the experience and lessons learned during the design and operation of a first-generation spacecraft simulator.[1] The latter was completely designed and built in-house under serious budgetary and time constraints. It is currently used mainly for educating undergraduate and graduate students. Compared to the first generation spacecraft simulator, the newly designed facility is heavily geared towards supporting advanced research in the area of nonlinear spacecraft control. To support this objective the facility has been equipped with a variety of different actuators and sensors: cold-gas (nitrogen) thrusters, variable-speed control moment gyros (VSCMG), sun sensor, magnetometer, rate gyro, and inertial measurement unit (IMU). The VSCMG's can operate either in reaction wheel (RW) or purely CMG mode, thus offering great flexibility in testing several attitude control laws. Most importantly, the VSCMG's allow experimental research relating to attitude control and energy storage of spacecraft in orbit.[2,3] Details on the sensors and actuators are given later in the paper.

The implementation of the attitude control algorithms is done via an on-board PC104 type Pentium computer that is interfaced with data acquisition and I/O cards. A high-speed wireless LAN connection enables remote command initiation, health monitoring and data collection for post-experimental analysis.

In this paper we present the major characteristics and the capabilities of the IACS. We briefly discuss some of the issues encountered during the initial operation of the simulator, such as motor parameter identification, noise, data accuracy and resolution, etc. The complete, nonlinear equations of the spacecraft are developed for the entire platform both for variable and fixed wheel configurations. Elimination of gravity torques necessitates operation of the platform in a completely balanced state (geometric center of rotation at the same location as the center of mass). A method is presented to estimate the moment of inertia (MOI) matrix and the location of the center of mass with respect to the center of rotation of the platform for the fixed wheel configuration. The simulation and experimental results based on a recursive estimation algorithm are provided. The results from the implementation of a nonlinear attitude stabilizing controller are shown.

Overview of the IACS Hardware

The "bus" of the spacecraft consists of a 32-in brass hub that sits on top of a hemi-spherical air bearing with 300 lbf vertical load capacity. The air-bearing has three rotational degrees of freedom: ± 30 deg about the x and y axes (horizontal) and 360 deg about the z axis (vertical). The platform itself contains various spacecraft components such as an on-board industrial computer, attitude and rate sensors, four variable speed CMG's (Controlled Momentum Gyros), pneumatic components for the cold-gas (nitrogen) thruster system, power supply system including two rechargeable batteries, etc. Figure 1 shows a schematic draw-

*Graduate Student, E-mail: dongwon_jung@ae.gatech.edu, Tel: (404) 894-6299, Fax: (404) 894-2760.

†Associate Professor, E-mail: p.tsiotras@ae.gatech.edu, Tel: (404) 894-9526, Fax: (404) 894-2760. Associate Fellow AIAA. Corresponding author.

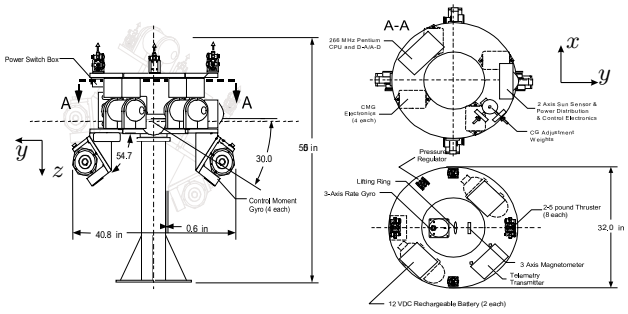

Fig. 1 A schematic drawing of the IACS spacecraft simulator facility.

ing of the simulator. Figure 2 shows a photograph of the actual facility.

The spacecraft platform is a cylindrical structure with two doughnut-shaped circular plates. This design was chosen among several others, because it is compact and offers great flexibility in mounting the spacecraft components. The location of the equipment on the platform has been as symmetric as possible, to allow easy balancing. Balancing of the platform is important in order to ensure a torque-free environment. An algorithm to estimate the center of gravity with respect to the center of rotation is presented later in the paper.

Fig. 2 The completed IACS spacecraft simulator.

Actuators

Thruster Reaction Control System: The Thruster Reaction Control System (TRCS) for the IACS consists of: eight adjustable, 5-lb (maximum) thrust jet valves grouped in two cluster pairs of three thrusters and two pairs of one thruster each; one manually adjustable pressure regulator; two 225-in^3 gas storage tanks; and supplementary filter and valves. Figure 3 illustrates the outline of the pneumatic system.

The two gas tanks are charged with high pressure nitrogen gas up to 2000 psi. The regulator provides

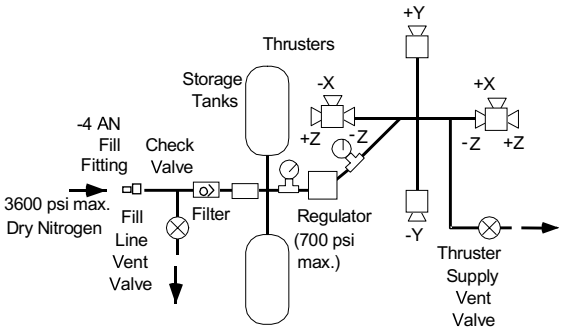

Fig. 3 Schematic of the thruster reaction control system (TRCS).

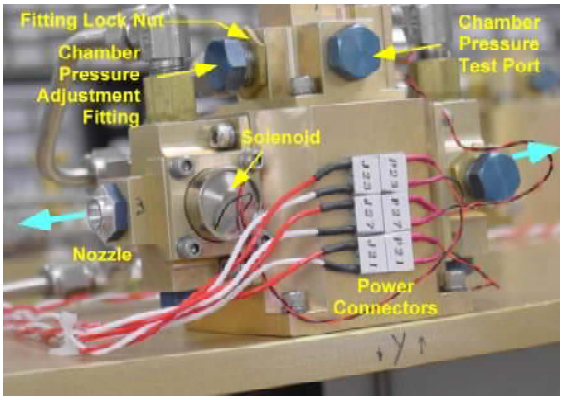

Fig. 4 Thruster module.

the operating pressure to each thruster valve by regulating the supplied high pressure. Two pairs of thrusters are arranged to generate reaction torques about the x and y body axes. The remaining four thrusters are responsible for the torque along the z-body axis. Each thruster module consists of a solenoid valve, outlet nozzle, pressure adjustment fitting, and pressure test port as shown in Fig. 4. The solenoid valve is driven by an amplified digital signal from the on-board computer, and the minimum operational pulse width is 15 ms, which corresponds to a bandwidth of the thruster of about 67 Hz. The thruster module allows the implementation of continuous torque via Pulse Width Pulse Modulate (PWPM) operation. The force exerted by the thruster can be set by adjusting the chamber pressure adjustment fitting. Figure 5 annotates the realization for the TRCS system on the IACS platform.

CMGs/VSCMGs: As illustrated in Fig. 6, each VSCMG module is composed of two brushless DC motors constructed by Hathaway Emoteq. One motor is used to control the gimbal. A potentiometer measures the gimbal rotation around the gimbal axis. The gimbal rate signal is also available to the user via a separate I/O channel. This motor operates in gimbal rate mode, via an internal servo loop. The gimbal

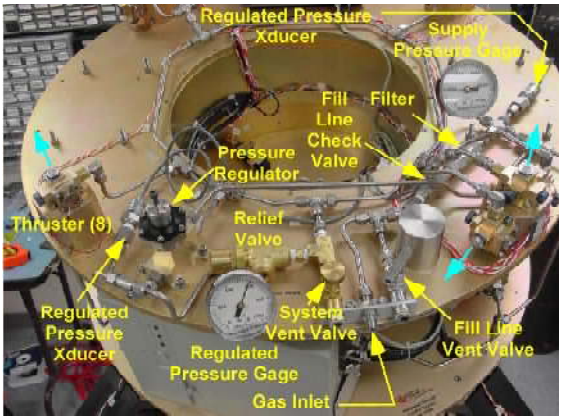

Fig. 5 The realization of the thruster reaction control system on the IACS platform.

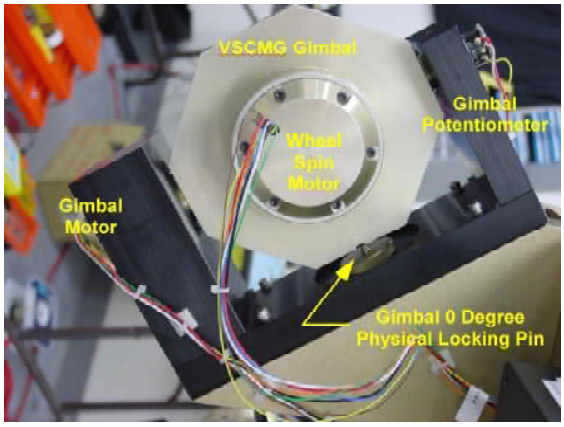

Fig. 6 Main components of the CMG/VSCMG.

is allowed to rotate within ±100 deg in accordance with the gimbal angular velocity command. The other brushless DC motor is coupled with the momentum wheel and provides torques along the wheel spin axis. Each wheel can be operated in either angular speed or torque command mode. An internal PID servo loop is being utilized in angular speed mode. However, there is no servo loop in the torque command mode and thus the spin motor operates in open-loop torque command mode. The details for the identification and modeling for both the gimbal and wheel (spin) DC motors are presented in the next section.

Each VSCMG can operate either in a purely CMG mode, a VSCMG mode or a Reaction Wheel (RW) mode. In the CMG mode, each CMG generates a maximum output torque of 170 mNm along the CMG output axis with a maximum sustained angular momentum of 1.76 Nms at a maximum wheel speed of 4000 RPM. In the VSCMG mode, each CMG generates a maximum output torque of 283 mNm along the spin axis with a maximum continuous output torque of 250 mNm. In addition, each VSCMG device can be used as a reaction wheel by locking down the gimbal angle to a fixed orientation. In this mode, the maximum reaction torque is 283 mN along the wheel rotation axis.

Sensors

Table 1 summarizes the specification of the sensors employed on the platform. The resolution level of each sensor was calculated along with the 1σ noise level. These values were obtained by measuring the sensor outputs while the platform was completely stationary and performing statistical analysis of the recorded data. It was found that all sensors performed within the limits specified by the manufacturers.

Sun Sensor: The sun sensor (by ACEi, Corp.) utilizes a sensor array that finds the average location of the brightest light spot in its field of view (±20 deg vertical/horizontal). It outputs an analog error signal between 1.5 Volt and 3.5 Volt for each axis. A signal of 2.5 Volt in both axes indicates the brightest point in the center of the field of view with an average scale factor of 44 mV/deg. The resolution level of the sun sensor is 0.05 deg and 1σ noise level is 0.05 deg.

Rate Gyro: A three-axes gyro rate sensor, RG02-3201 by Humphrey, Inc. provides direct measurements of the inertial angular velocities with respect to the body fixed frame. The range of the angular rate is ±30 deg/sec in each axis and the corresponding output voltage range is ± 2.5 V. The resolution level of the gyro is 0.029 deg/sec and 1σ noise level is 0.027 deg/sec.

Magnetometer: In order to detect the orientation of the IACS, a magnetometer (FM02-0101 by Humphrey Inc.) can be used. The magnetometer provides three analog signals corresponding to the strength of the magnetic field along the magnetometer axes. Since the Earth's magnetic field can be assumed constant over the time of the experiments, these measurements can be processed with the rate measurements to find the relative orientation of IACS platform with respect to the Earth. The resolution level of the magnetometer is 0.0006 Gauss and 1σ noise level is 0.0002 Gauss.

Dynamic Measurement Unit: An additional inertial measurement unit (DMU-Dynamic Measurement Unit by Crossbow, Inc., Model DMU-AHRS) has been installed on the IACS platform to supplement the RG02-3201 rate gyro and the sun sensor/magnetometer. It can serve as a back-up device and for the moment it is used to cross-validate and debug the facility during the initial stages of its operation. Internally, the DMU-AHRS combines linear accelerometers, rotational rate sensors, and magne-

Table 1 Sensor specifications of the IACS.

Sensors		Available Range	Min. Resolution	1σ noise	Remarks
DMU	Accelerometer	$\pm$2g	0.001g	0.0015g	1g=9.81m/sec^2
	rate gyro	$\pm$150	0.073	0.17	deg/sec
	magnetometer	$\pm$1.25	0.0006	0.001	gauss
RG02-32 Rate gyro		$\pm$30	0.029	0.027	deg/sec
FM02 Magnetometer		$\pm$0.5	0.0005	0.0002	gauss
Sun sensor		$\pm$20	0.05	0.05	Deviation angle, deg
Regulated pressure X-ducer		1000	1.394	0.696	psi
Supply pressure X-ducer		5000	2.929	1.582	psi
CMG	Gimbal position	$\pm$100	0.1563	0.6	deg
	Gimbal Rate	$\pm$22	0.02	0.25	deg/sec
	Rotor speed	3500	3	33	rpm

tometers with a Digital Signal Processor (DSP) unit to produce application-specific outputs such as Euler angles, compensating for deterministic error sources within the unit. With this feature, it can measure roll and pitch angles of $\pm 90°$ and a heading angle of $\pm 180°$. The angular rate range is $\pm$150 deg/sec and the accelerometer range is $\pm$2 g. The DMU measurement data are sent to the host computer via an RS-232 serial port.

On-board Computer and I/O Boards

An industrial embedded computer (ADLink NuPRO-775 Series) is used for data acquisition, data recording, and controller implementation via the MATLAB xPC Target Environment® with Embedded Option.[4] The main CPU, is based on the Intel Pentium® III 750MHz processor with on-board memory 128MB DRAM and 128MB disk-on-chip, allows a user for real-time data acquisition, processing, and data recording. The connection to the host computer is done in the xPC Target Environment via wireless Ethernet LAN connection. The wireless LAN router (DLink DI-713P) and the USB adapter (DLink DWL-120) make it possible to transfer data at speeds up to 11Mbps.

The target computer system has three data acquisition interface cards installed. Two analog input cards (PCI-6023E from National Instruments) are used to measure the analog voltages from the rate gyro, magnetometer, and sun sensor. Another analog output card (PCI-6703 from National Instruments) is used to control the VCMGs. In addition, a digital I/O function in the PCI-6023E card generates commands for the thruster valves and the CMG/RW mode changing commands.

Table 2 summarizes the performance specifications of the IACS.

DC Motor Modeling

Gimbal Motor Modeling

Each gimbal of the VSCMG is controlled by a gimbal rate command ($\dot{\gamma}_c$) utilizing an internal PID servo loop. Figure 7 depicts the gimbal rate response to a series of step commands. From this figure, it is evident that the PID servo achieves a first-order system response. The transfer function from gimbal rate command to gimbal rate was thus modelled as a first-order system with gain $K = 1.0102$ and time constant $\tau = 0.6617$.

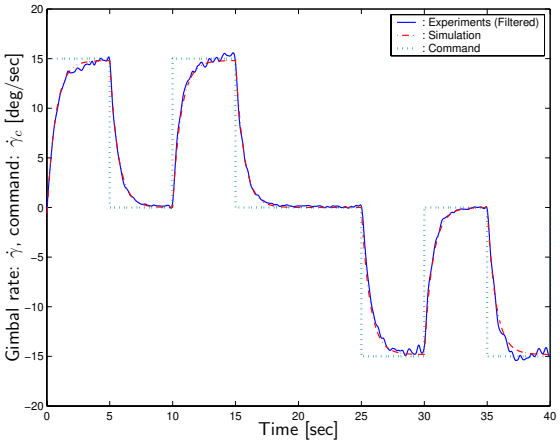

Fig. 7 Gimbal response: simulation and experimental response of gimbal rate for a series of step commands.

Wheel Motor Modeling

In VSCMG/RW mode, the motor is controlled by a torque command in open-loop mode. Since there is no torque servo loop, it was deemed necessary to model the whole motor dynamics accurately. To this end, a high-fidelity SIMULINK diagram was constructed taking into account all the significant parameters that affect the motor performances.

The equations of motion of a conventional DC motor with a combined motor/rotor moment of inertia I_w with Coulomb and viscous friction are given as fol-

Table 2 IACS design specifications.

Performance parameter	Value	Remarks
Total Weight	295 lbs	maximum
Moment of Inertia (I_x)	13 kg-m^2	estimated
Moment of Inertia (I_y)	13 kg-m^2	estimated
Moment of Inertia (I_z)	18 kg-m^2	estimated
CMG Output Torque (per wheel)	280 mNm	3000 RPM, ($\dot{\gamma}$) = 13.3 deg/s
CMG Angular Momentum (per wheel)	1.76 Nms	4000 RPM
Thruster torque (X-axis)	2.36 Nm	maximum
Thruster torque (Y-axis)	2.36 Nm	maximum
Thruster torque (Z-axis)	4.71 Nm	maximum
CMG/RW Acceleration (X-axis)	1.22 deg/s^2	2 CMGs/Single RW @1500 RPM
CMG Acceleration (Y-axis)	1.26 deg/s^2	2 CMGs
CMG Acceleration (Z-axis)	1.8 deg/s^2	2 CMGs
RW Acceleration (X-axis)	1.06 deg/s^2	Single RW @1500 RPM
RW Acceleration (Y-axis)	1.10 deg/s^2	Single RW @1500 RPM
RW Acceleration (Z-axis)	1.1 deg/s^2	Two RWs 1500 RPM
Thruster Acceleration (X-axis)	8.44 deg/s^2	Average set level
Thruster Acceleration (Y-axis)	6.01 deg/s^2	Average set level
Thruster Acceleration (Z-axis)	7.35 deg/s^2	Average set level

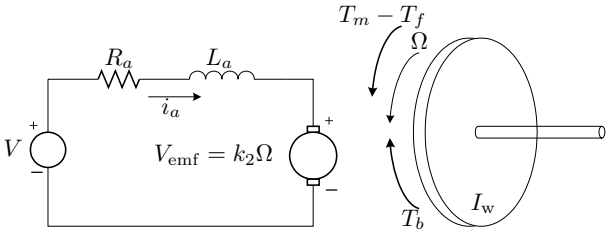

Fig. 8 Electronic circuit of the armature and free-body diagram of the wheel DC motor.

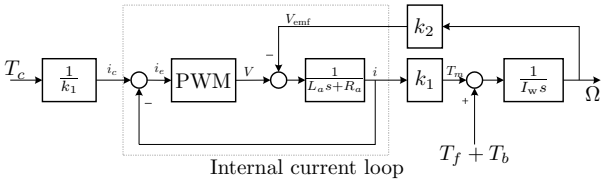

Fig. 9 Wheel motor open-loop torque control diagram.

lows[5]

$$\begin{aligned} T_m &= k_1 i_a \\ V_{\text{emf}} &= k_2 \Omega \\ V - V_{\text{emf}} &= R_a i_a + L_a \frac{\mathrm{d}i_a}{\mathrm{d}t} \\ T_m + T_f + T_b &= I_{\text{w}} \dot{\Omega} \end{aligned}$$

where T_m is the torque generated by the motor coil, T_f is the friction torque (Coulomb and viscous) on the bearing and motor itself, and T_b is the braking disturbance torque appearing during the operation of motor. The motor parameters are given by k_1 (torque constant), k_2 (speed constant), R_a (resistance of the armature coil), L_a (inductance of armature coil), and i_a (armature coil current). A schematic of the DC motor dynamics is shown in Fig. 8. The wheel motor is controlled by the open-loop torque command as illustrated in Fig. 9. The internal current loop forces the current on the coil to follow the current command while rejecting the back-EMF voltage. However, since there also exists a disturbance torque due to friction and electromagnetic-power braking, the effective torque delivered to the wheel is not identical to the commanded torque. Figure 10 shows the open-loop response of the wheel motor to a step command. The angular acceleration command ($\dot{\Omega}_c$) is applied and the actual wheel angular acceleration and angular velocity were measured. It is evident that due to the disturbance torques the actual $\dot{\Omega}$ differs from the commanded $\dot{\Omega}$.

Friction modeling

The friction existing on the motor itself and the bearings can be modelled by Coulomb and viscous friction as follows,

$$T_f = \begin{cases} -T_s - b\Omega & \text{if } \Omega \neq 0 \\ -T_s & \text{if } \Omega = 0 \text{ and } |T_m| > |T_s| \\ -T_m & \text{if } \Omega = 0 \text{ and } |T_m| \leq |T_s| \end{cases}$$

where, $T_s = \text{sign}(\Omega) \cdot T_{s_0}$ is Coulomb friction on the motor/bearing with the friction constant T_{s_0} and b is viscous friction coefficient for each motor/bearing. The Coulomb friction can be identified by applying small nonzero torque command that forces the wheel to start rotate. Since there exists a pre-fixed constant dead-zone level on the torque command in order to prevent the motor from noisy operation near zero torque command, the Coulomb friction is identified in the following manner:

$$T_{s_0} = k_1(T_a - T_{\text{dz}})$$

where, T_a is the applied torque command at the verge of rotation and T_{dz} is the dead-zone torque command

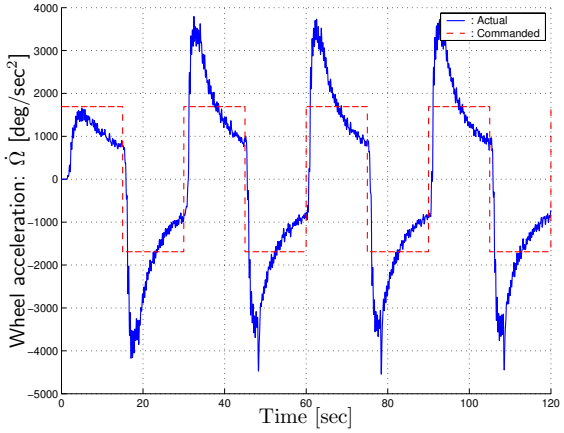

a) Wheel Acceleration $\dot{\Omega}$.

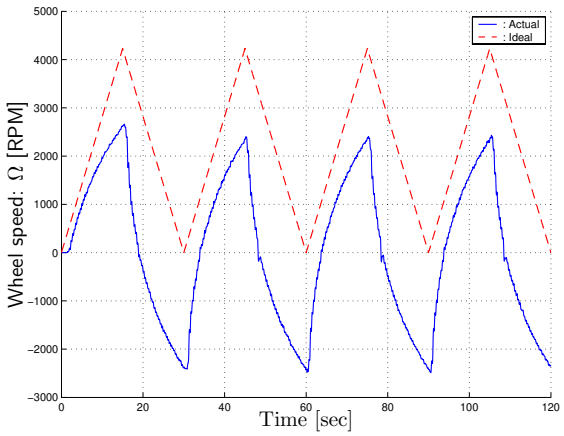

b) Wheel Speed Ω.

Fig. 10 Wheel open-loop response: $\dot{\Omega}$ and Ω

Table 3 Friction identification

Motor	Coulomb [Nm]	Viscous [Nm/rad/sec]
CMG#1	6.67e-3	1.02e-4
CMG#2	1.42e-3	1.03e-4
CMG#3	1.91e-3	0.92e-4
CMG#4	1.02e-3	0.99e-4

level. Next, in order to identify the viscous friction coefficient of the motor/bearing, the wheel was spun up to some high speed and then motor/wheel was left to decelerate slowly due to the friction torque. Since the back-EMF voltage causing magnetic damping is regulated properly inside the current loop during deceleration, and the inertia of the wheel is accurately known, one can estimate the viscous friction coefficient. Figure 11 shows the results from these experiments. The plots show the friction torque amplitude vs. angular velocity. It can be inferred that the viscous friction coefficient is the slope of the regressed line. Table 3 summarizes the identified friction.

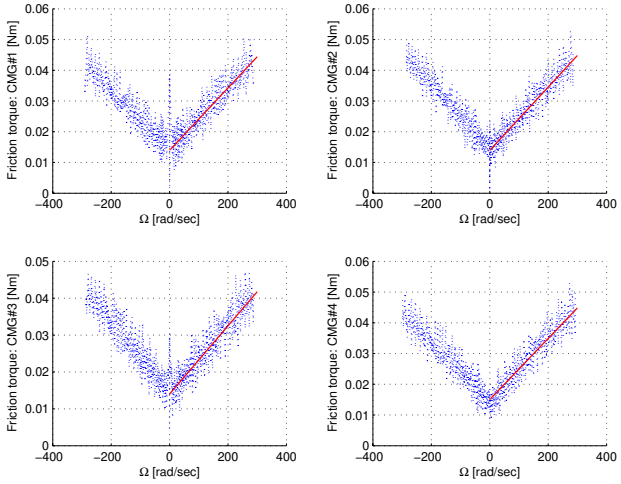

Fig. 11 Friction torque versus speed during deceleration

Braking torque modeling[6]

The PWM amplifier for the wheel motor uses two distinct modes of operation. In the normal mode the torque command and the angular speed have the same polarity. In this normal mode the motor generates a torque according to the torque command. If, on the other hand, the torque command and the angular speed have opposite polarities, a so-called "braking" torque is generated. This braking torque results in a large deceleration of the motor that is not directly evident by the DC model dynamics. The braking torque is the result of the power electronics driving the motor coil. When the torque and the current command have different signs, the motor acts as a generator. Due to the back-EMF a large voltage appears at the driving circuit port. It is necessary to drain this reversal current off so as to protect the motor circuit from severe damage. This is done by short-circuit the electronics and "damping" the excess power to the load. The result a large additional disturbance decelerating torque.

In order to capture this effect, the braking torque was modelled as follows,

$$T_b = \begin{cases} -\text{sign}(i_c) \cdot k_b |\Omega| & \text{if } \Omega \cdot i_c < 0 \\ 0 & \text{if } \Omega \cdot i_c \geq 0 \end{cases}$$

where, i_c is the current command which is referenced by the internal current loop and k_b is the coefficient of the braking torque.

Open-loop model validation

A SIMULINK model for each motor wheel from torque command to wheel velocity Ω was built based on the known motor parameters. The internal current on/off (PWM) controller block was replaced by an equivalent proportional block with a carefully chosen gain value. The friction and braking torques were

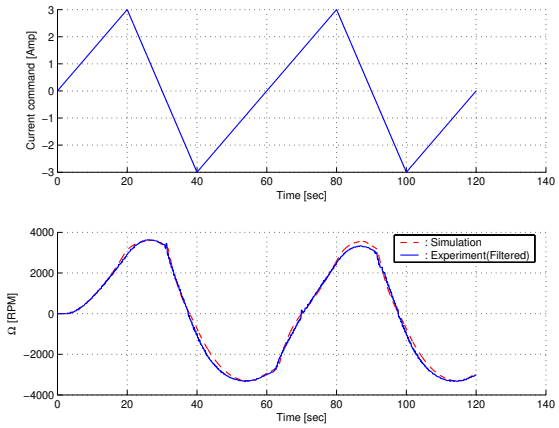

a) Ramp command.

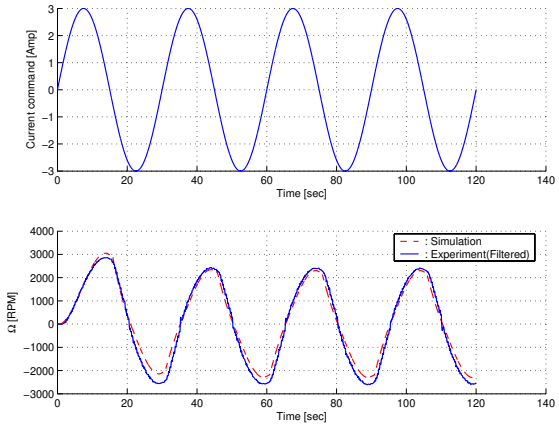

b) Sinusoidal command.

Fig. 12 Validation of SIMULINK open-loop model

also included in the model based on the experimental results. Assuming that the motor parameters are close to the nominal values, all other unknown parameters were then carefully chosen to match the simulations with the experimental results. After identification, a second series of experiments was performed (with different commands) to validate the model. The results of these experiments are shown in Fig. 12. At this point it was decided that the wheel DC motor model was accurate enough for our purposes.

Implementation of a servo loop for wheel acceleration

Since the wheel motors operate in open-loop torque command, it is necessary to implement a servo loop that controls the angular acceleration of the wheel ($\dot{\Omega}$) corresponding to the torque command. A simple proportional-integral (PI) servo loop for $\dot{\Omega}$ was implemented utilizing the available signal Ω as shown in Fig. 13. Since the angular velocity Ω is noisy, the derivative signal $\dot{\Omega}$ that is necessary for implementation of PI loop was obtained using the pseudo-differentiator transfer function $\frac{s}{\tau s+1}$ with carefully

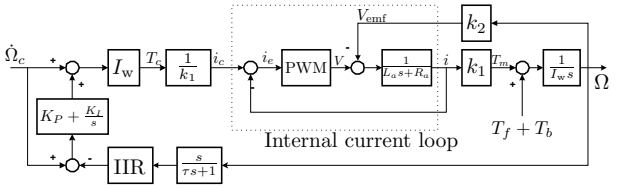

Fig. 13 Implementation of PI servo loop

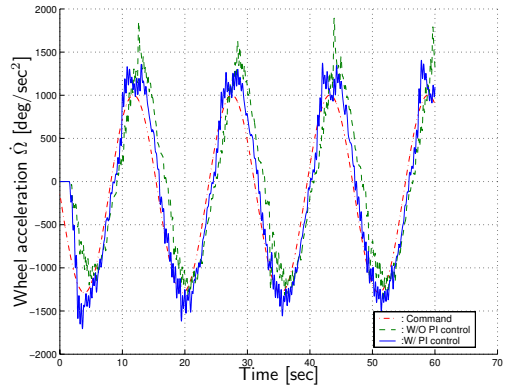

a) Wheel acceleration $\dot{\Omega}$

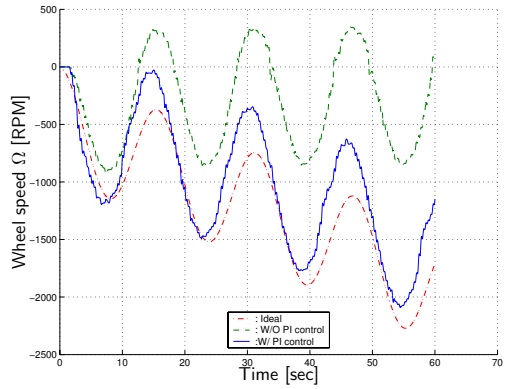

b) Wheel speed Ω

Fig. 14 The PI controller performance: comparison between Open-loop and Closed-loop

chosen time constant τ considering the system bandwidth. The discrete IIR low pass filter follows the differentiator so as to get clean derivative signal. A 4th order Butterworth low pass filter was adopted with cutoff frequency 3Hz. Even though the PI servo loop manages to reduce the error between command and actual $\dot{\Omega}$ due to the disturbance torque, the selection of PI gains is restrictive because of the noisy Ω signal. The delay introduced by the denoising filter may lead to an unstable loop. Thus the PI gains and the denoising filter characteristics were chosen carefully after trial and error so that the closed-loop is stable, while achieving acceptable performance (settling time, overshoot etc). Figure 14 shows the experimental results from the implementation of the PI loop.

Equations of Motion

The equations of motion for a rigid spacecraft with a cluster of N variable speed CMGs have been developed in Ref. 3. We repeat them here for convenience

$$\begin{aligned}\Big(A_{\rm t}[\dot\gamma]^d(I_{\rm cs}-I_{\rm ct})A_{\rm s}^T + A_{\rm s}[\dot\gamma]^d(I_{\rm cs}-I_{\rm ct})A_{\rm t}^T\Big)\omega + J\dot\omega \\ + A_{\rm g}I_{\rm cg}\ddot\gamma + A_{\rm t}I_{\rm ws}[\Omega]^d\dot\gamma + A_{\rm s}I_{\rm ws}\dot\Omega \\ + [\omega^\times]\Big(J\omega + A_{\rm g}I_{\rm cg}\dot\gamma + A_{\rm s}I_{\rm ws}\Omega\Big) = 0\end{aligned} \tag{1}$$

In Eq. (1) $\omega = (p,q,r)^T \in \mathbb{R}^3$ is the spacecraft angular velocity vector expressed in the body frame. The matrix J is the inertia matrix of the whole spacecraft, defined as

$$J := {}^BI + A_{\rm s}I_{\rm cs}A_{\rm s}^T + A_{\rm t}I_{\rm ct}A_{\rm t}^T + A_{\rm g}I_{\rm cg}A_{\rm g}^T \tag{2}$$

where ${}^BI$ is the combined matrix of inertia of the spacecraft platform and the point-masses of the VSCMGs. The matrices $I_{\rm c\star}$ and $I_{\rm w\star}$ are diagonal with elements the values of the inertias of the gimbal plus wheel structure and wheel-only-structure of the VSCMGs, respectively. Specifically, $I_{\rm c\star} := I_{\rm g\star} + I_{\rm w\star}$ where $I_{\rm g\star} := {\rm diag}[I_{\rm g\star_1},\ldots,I_{\rm g\star_N}]$ and $I_{\rm w\star} := {\rm diag}[I_{\rm w\star_1},\ldots,I_{\rm w\star_N}]$, where $\star$ is g, s or t. The vectors $\gamma = (\gamma_1,\ldots,\gamma_N)^T \in \mathbb{R}^N$ and $\Omega = (\Omega_1,\ldots,\Omega_N)^T \in \mathbb{R}^N$ have elements the gimbal angles and the wheel speeds of the VSCMGs with respect to the gimbals, respectively. The matrices $A_\star \in \mathbb{R}^{3\times N}$ have as columns the gimbal, spin and transverse unit vectors expressed in the body-frame. Thus, $A_\star = [e_{\star 1},\cdots,e_{\star N}]$, where $e_{\star j}$ is the unit column vector for the jth VSCMG along the direction of the gimbal, spinning, or transverse axis. Note that $A_{\rm s} = A_{\rm s}(\gamma)$ and $A_{\rm t} = A_{\rm t}(\gamma)$ and thus, both matrices $A_{\rm s}$ and $A_{\rm t}$ are functions of the gimbal angles. Consequently, the inertia matrix $J = J(\gamma)$ is also a function of the gimbal angles γ, whereas the matrix ${}^BI$ is constant. For any vector $x = (x_1,x_2,x_3)^T \in \mathbb{R}^3$, the notation $[x^\times]$ denotes the skew-symmetric matrix

$$[x^\times] := \begin{bmatrix} 0 & -x_3 & x_2 \\ x_3 & 0 & -x_1 \\ -x_2 & x_1 & 0 \end{bmatrix}$$

whereas, for the vector $x \in \mathbb{R}^N$ the notation $[x]^d \in \mathbb{R}^{N\times N}$ denotes a diagonal matrix with its elements the components of the vector x, i.e.,

$$[x]^d := {\rm diag}(x_1,\cdots,x_N)$$

Equations of Motion for RW Mode

Later we provide an algorithm for estimating the moment of inertia (MOI) matrix of the spacecraft platform. For the purposes of the MOI identification the four CMGs were fixed to an angle of 90 deg. In this configuration the spacecraft was operated in a reaction wheel mode and the moment of inertia matrix of the entire spacecraft (including the wheels and gimbal structure) is constant. The applied torques from the wheels are also fixed in the spacecraft frame (along the fixed wheel spin axes). The only external torque acting on the system results from the possible misalignment of the mass center from the center of rotation given by

$$\vec{T}_{\rm ext} = \vec{r}_c \times mg\vec{K} \tag{3}$$

where $\vec{r}_c$ is the position vector from the center of rotation of the platform to the center of mass, and $\vec{K}$ is the inertial unit vector along the vertical (Z-axis of inertial frame points down). With these simplifications, the equations of motion of the platform in RW mode are given by

$$J\dot\omega + A_{\rm s}I_{\rm ws}\dot\Omega + [\omega^\times]\left(J\omega + A_{\rm s}I_{\rm ws}\Omega\right) = \{\vec{T}_{\rm ext}\}_{\mathcal{B}} \tag{4}$$

where $\{\cdot\}_{\mathcal{B}}$ denotes the column vector expressed in terms of the unit vectors of the frame $\mathcal{B}$.

Kinematics

In order to describe the attitude of spacecraft, the conventional 3-2-1 Euler angle sequence is used. The relevant direction cosine matrix used to transform vectors from the inertial frame to the spacecraft frame is given by

$$R^{\mathcal{BI}} = \begin{bmatrix} {\rm c}_\theta{\rm c}_\psi & {\rm c}_\theta{\rm s}_\psi & -{\rm s}_\theta \\ {\rm s}_\phi{\rm s}_\theta{\rm c}_\psi - {\rm c}_\phi{\rm s}_\psi & {\rm s}_\phi{\rm s}_\theta{\rm s}_\psi + {\rm c}_\phi{\rm c}_\psi & {\rm s}_\phi{\rm c}_\theta \\ {\rm c}_\phi{\rm s}_\theta{\rm c}_\psi + {\rm s}_\phi{\rm s}_\psi & {\rm c}_\phi{\rm s}_\theta{\rm s}_\psi - {\rm s}_\phi{\rm c}_\psi & {\rm c}_\phi{\rm c}_\theta \end{bmatrix} \tag{5}$$

The kinematic equations are given by

$$\begin{bmatrix}\dot\phi\\ \dot\theta\\ \dot\psi\end{bmatrix} = \begin{bmatrix} 1 & \sin\phi\tan\theta & \cos\phi\tan\theta \\ 0 & \cos\phi & -\sin\phi \\ 0 & \sin\phi/\cos\theta & \cos\phi/\cos\theta \end{bmatrix}\begin{bmatrix}p\\ q\\ r\end{bmatrix} \tag{6}$$

Moment of Inertia Matrix Estimation

Regression equations

The equations of motion of the spacecraft platform in RW mode are given by Eqs. (3), (4) and (6). Let us rewrite (4) as follows

$$J\dot\omega + [\omega^\times]J\omega + A_{\rm s}I_{\rm ws}\dot\Omega + [\omega^\times]A_{\rm s}I_{\rm ws}\Omega = -mg[\{\vec{K}\}_{\mathcal{B}}^\times]\{\vec{r}_c\}_{\mathcal{B}} \tag{7}$$

In order to put this equation in a regression form, needed for the MOI identification algorithm, we first note that the unit vector $\vec{K}$ when expressed in the spacecraft frame $\mathcal{B}$ is given by

$$\{\vec{K}\}_{\mathcal{B}} = \begin{bmatrix} -\sin\theta \\ \sin\phi\cos\theta \\ \cos\phi\cos\theta \end{bmatrix} \tag{8}$$

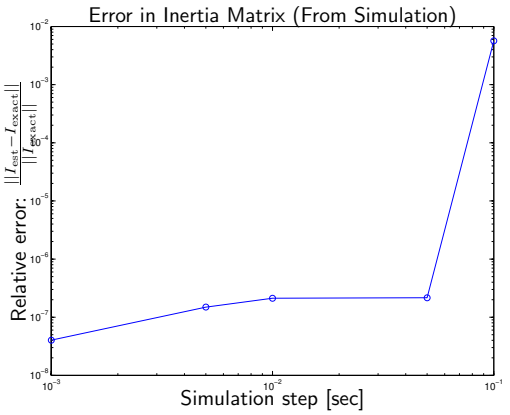

Fig. 15 Verification of estimation equations by simulation

Let also $\{\vec{r}_c\}_{\mathcal{B}} = (r_x, r_y, r_z)^T$ be the components of the vector $\vec{r}_c$ expressed in the body frame. Substituting these expressions in (7) yields an expression of the form

$$\mathcal{A}\mathcal{X} = \mathcal{T} \tag{9}$$

where the unknown parameter vector to be estimated is given by

$$\mathcal{X} := \begin{bmatrix} I_x & I_{xy} & I_{xz} & I_y & I_{yz} & I_z & mgr_x & mgr_y & mgr_z \end{bmatrix}^T$$

Given the regression form (9), a recursive least-square parameter estimation algorithm[7] was used to estimate the unknown vector $\mathcal{X}$.

In order to verify the regression equation and examine the numerical error of the recursive estimation, a simulation for the estimation algorithm was performed on the basis of the dynamics equation and kinematics. There is no noise on the measurement channels in the simulation, thus one can assume that the only error affecting the estimation algorithm is the numerical error from the simulation time step. Simulations were performed in MATLAB using fourth order Runge-Kutta formulas with various time steps. Figure 15 shows the estimated relative error with respect to the simulation time step. As shown in the figure, the relative error is small and decreases as the simulation time step decreases. Thus, we concluded that the numerical error of the recursive algorithm is negligible a fixed simulation step of 0.005 [sec] (sampling rate of 200Hz) was used.

Robust Nonlinear Stabilization Controller

During the MOI estimation, an excitation is necessary for the regressor matrix to be non-singular. However, since the air-bearing structure limits the rotation angles of the platform in the roll and pitch axes within ±30 deg, a stabilizing controller was turned on in order to prevent the platform from hitting the safety stops. Because the moment of inertia matrix J is unknown, a nonlinear robust stabilizing controller that does not require knowledge of J was implemented together with the estimation algorithm.

The stabilizing controller in Ref. 8 has been derived for the following dynamic equation of a rigid spacecraft.

$$J\dot{\omega} + [\omega^\times]J\omega = u \tag{10}$$

The stabilizing controller, taken from Ref. 8, is given by

$$u = -\frac{1}{2}\left[(\bar{\alpha}^\times + \alpha_4 \mathbf{1}_3)G_p + \gamma(1-\alpha_4)\mathbf{1}_3\right]\bar{\alpha} - G_r\omega \tag{11}$$

where, G_p and G_r are positive definite gain matrices, $0 < \lambda_{max}(G_p) \leq 2\gamma$, and $\mathbf{1}_3$ is the 3×3 identity matrix. In (11) the vector $\alpha := (\bar{\alpha}^T, \alpha_4)^T$ is the Euler parameter vector defined as usual, by[9]

$$\bar{\alpha} := \begin{bmatrix} \alpha_1 \\ \alpha_2 \\ \alpha_3 \end{bmatrix} \sin\frac{\Phi}{2}, \qquad \alpha_4 := \cos\frac{\Phi}{2} \tag{12}$$

where $\hat{\alpha} := (\alpha_1, \alpha_2, \alpha_3)^T$ is the unit vector along the eigen-axis of rotation and Φ is the magnitude of rotation. Notice that the four-dimensional Euler parameter vector satisfies the constraint $\bar{\alpha}^T\bar{\alpha} + \alpha_4^2 = 1$.

The dynamic equation of motion in case of momentum/reaction wheels neglecting the gravity torque is given as follows

$$J\dot{\omega} + [\omega^\times]J\omega + A_s I_{ws}\dot{\Omega} + [\omega^\times]A_s I_{ws}\Omega = 0 \tag{13}$$

Then, by comparing (10)-(13) we can reformulate the stabilizing control law in the following form:

$$\begin{aligned}\dot{\Omega}_c = &-(A_s I_{ws})^\dagger\Big[\omega \times A_s I_{ws}\Omega \\ &- \frac{1}{2}[(\hat{\bar{\alpha}} + \alpha_4 I)G_p + \gamma(1-\alpha_4)I]\bar{\alpha} - G_r\omega\Big]\end{aligned} \tag{14}$$

where, $\dot{\Omega}_c \in \mathbb{R}^4$ is the control command to the wheel motors and $(\cdot)^\dagger$ implies the pseudo-inverse of a matrix.

Since the on-board sensors provide Euler angles as the attitude signals, the following equations were used to convert the Euler angles to the Euler parameters,[9] required for implementing the controller in (14)

$$\begin{aligned}\alpha_1 &= \sin\frac{\phi}{2}\cos\frac{\theta}{2}\cos\frac{\psi}{2} - \cos\frac{\phi}{2}\sin\frac{\theta}{2}\sin\frac{\psi}{2} \\ \alpha_2 &= \cos\frac{\phi}{2}\sin\frac{\theta}{2}\cos\frac{\psi}{2} + \sin\frac{\phi}{2}\cos\frac{\theta}{2}\sin\frac{\psi}{2} \\ \alpha_3 &= \cos\frac{\phi}{2}\cos\frac{\theta}{2}\sin\frac{\psi}{2} - \sin\frac{\phi}{2}\sin\frac{\theta}{2}\cos\frac{\psi}{2} \\ \alpha_4 &= \cos\frac{\phi}{2}\cos\frac{\theta}{2}\cos\frac{\psi}{2} + \sin\frac{\phi}{2}\sin\frac{\theta}{2}\sin\frac{\psi}{2}\end{aligned} \tag{15}$$

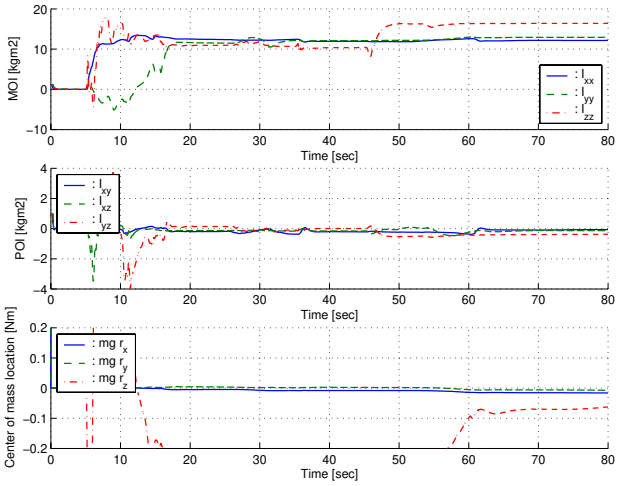

Fig. 16 Estimation of mass properties from experiments

Table 4 Estimation results (Experiment)

Average Estimates: Experiment	
Inertia matrix J, [kgm^2]	SD $\sigma(J)$, [kgm^2]
$\begin{bmatrix} 12.2012 & -0.0899 & -0.0469 \\ -0.0899 & 12.9943 & -0.4187 \\ -0.0469 & -0.4187 & 16.2764 \end{bmatrix}$	$\begin{bmatrix} 0.052 & 0.029 & 0.057 \\ 0.029 & 0.071 & 0.021 \\ 0.057 & 0.021 & 0.101 \end{bmatrix}$
Gravity vector mgr_i, [Nm]	SD $\sigma(mgr_i)$, [Nm]
$\begin{bmatrix} -0.0163 & -0.0067 & -0.0661 \end{bmatrix}^{\mathrm{T}}$	$\begin{bmatrix} 0.0005 & 0.0006 & 0.0041 \end{bmatrix}^{\mathrm{T}}$

Simulation and Experimental Results

Estimation of Mass Properties

The mass properties, MOI matrix and gravity vector of the IACS platform, were estimated through the method described in the former section. In order to get the most reliable estimation results it was necessary to excite the platform in such a manner that makes the regressor matrix well-conditioned. Then the platform was stabilized to a horizontal level by turning on the stabilizing controller. The estimation process continues consecutively with another excitation followed by stabilization, and so on.

The experiments for the estimation of the inertia properties of the IACS platform were performed along the maneuver described above. Figure 16 shows the estimation results from the experiments and Table 4 gives the final estimated values. The final estimates and their standard deviations are taken from the final portion of the data when their relative changes are small and the condition number of the regressor matrix settles near its minimum. (See Fig. 17)

Nonlinear stabilizing controller

A SIMULINK model of the whole spacecraft dynamics was constructed with all subsystems included. The SIMULINK model reflects the actual system closely, and it can be used as a reference model for future development of sophisticated control algorithms on the platform. This model was further validated by implementing the stabilizing controller described in previous section. The position gain G_p, rate gain G_r, and γ of the stabilizing controller were carefully chosen for good performance as follows:

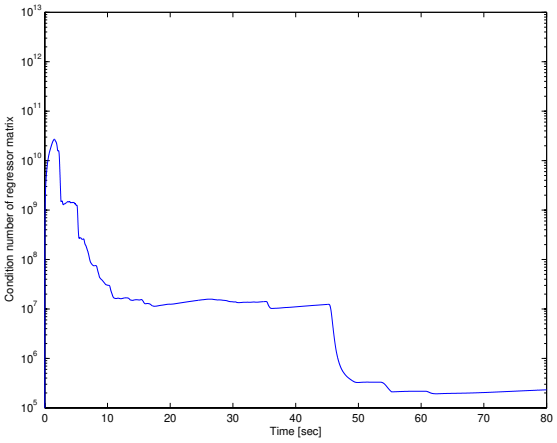

Fig. 17 Condition number of the regressor matrix during MOI estimation

$$G_p = \mathrm{diag}([6.3,\ 6.3,\ 7.2])$$
$$G_r = \mathrm{diag}([5,\ 5,\ 8])$$
$$\gamma = 5$$

Before the implementation of any attitude stabilizing controller, it is very important to balance the system in order to emulate a torque-free environment. Unless the platform is well balanced, the gravity torque resulting from the mismatch of the center of mass location with respect to the center of rotation would generate extra control action. This may lead to saturation of the actuators. Before the experiments the system was balanced as close as possible to a torque-free state. Then the estimates of the center of mass location with respect to the center of rotation were included in the simulation to verify the model. Figures 18-21 compare the experimental and simulation results. The results show very good correlation between experimental and simulated responses.

Conclusions

We have presented the details of a state-of-the-art experimental facility for the development, validation and testing of attitude determination and control algorithms. This facility will be indispensable for attitude control research conducted at Georgia Tech. The experimental spacecraft simulator incorporates a wide variety of sensors and actuators which allows testing of several sensor/actuator configurations. The whole system is modelled accurately so as to reproduce the actual system to a high degree of fidelity. The MOI

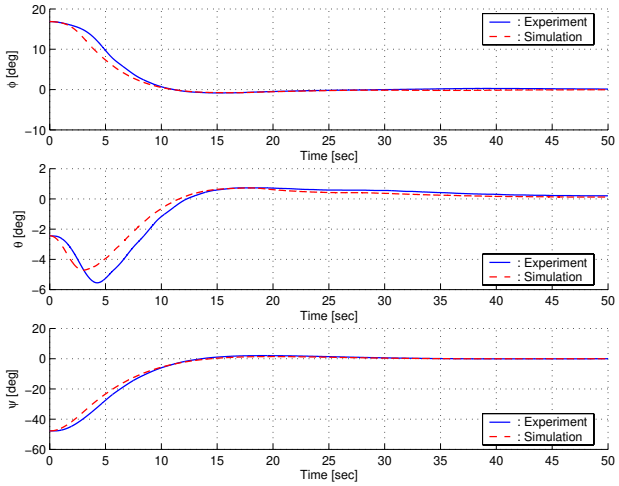

Fig. 18 Attitude angle ϕ, θ, ψ

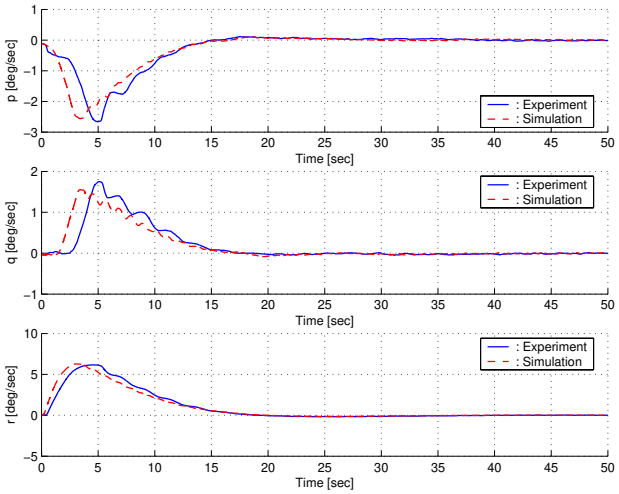

Fig. 19 Body angular rate p, q, r

matrix and the center of mass location were identified through an online recursive estimation algorithm. Based on the complete model, a nonlinear attitude stabilizing controller was implemented to verify the model validity. The results show very good correlation between experimental and simulated responses.

Acknowledgment: This work has been supported by AFOSR grant no. F49620-00-1-0374 and DURIP/AFOSR grant no. F49620-01-1-0198.

References

[1]Kim, B., Velenis, E., Kriengsiri, P., and Tsiotras, P., "A Spacecraft Simulator For Research And Education," *AAS/AIAA Astrodynamics Conference*, Quebec City, Canada, 2001, Paper AAS 01-367.

[2]Tsiotras, P., Shen, H., and Hall, C., "Satellite Attitude Control and Power Tracking with Momentum Wheels," *Journal of Guidance, Control, and Dynamics*, Vol. 24, No. 23–34, 2001.

[3]Yoon, H. and Tsiotras, P., "Spacecraft Adaptive Attitude and Power Tracking with Variable Speed Control Moment Gyroscopes," *Journal of Guidance, Control and Dynamics*, Vol. 25, No. 6, 2002, pp. 1081–1090.

[4]Mathworks, "xPC Target User's Guide," On-line document, http://www.mathworks.com/, 2001.

[5]Franklin, G. F., Powell, J. D., and Emami-Naeini, A., *Feedback Control of Dynamic Systems*, Addison Wesley, 3rd ed., 1995.

[6]Becerra, R. C. and Jahns, T. M., "Four-Quadrant Brushless ECM Drive with Integrated Current Regulation," *IEEE Transactions on Industry Applications*, Vol. 28, No. 4, 1992, pp. 833–841.

[7]Åström, K. J. and Wittenmark, B., *Adaptive Control*, Addison Wesley, 2nd ed., 1995.

[8]Joshi, S. M., Kelkar, A. G., and Wen, J. T. Y., "Robust Attitude Stabilization of Spacecraft Using Nonlinear Quaternion Feedback," *IEEE Transactions on Automatic Control*, Vol. 4, No. 10, 1995, pp. 1800–1803.

[9]Hughes, P. C., *Spacecraft Attitude Dynamics*, John Wiley & Sons, New York, 1986.

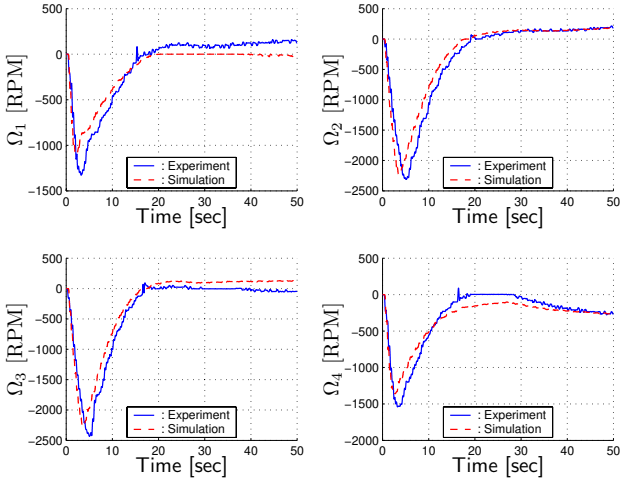

Fig. 20 Wheel angular velocity Ω

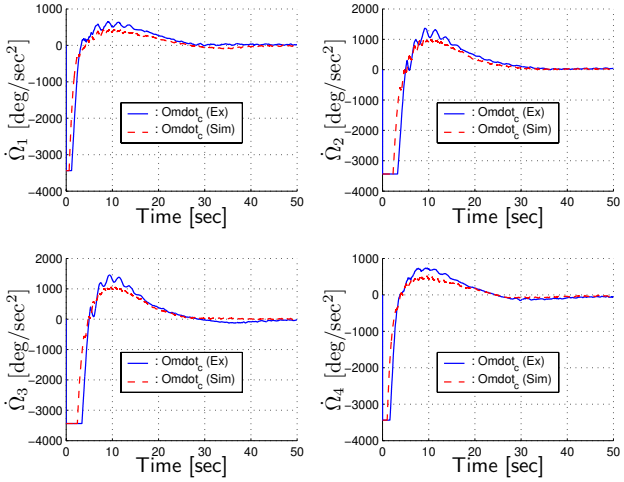

Fig. 21 Control command to each wheel motor $\dot{\Omega}_c$